International Journal of Fluid Engineering 国际流体工程(英文)

RESEARCH ARTICLE | OCTOBER 16 2024

Dynamics and energy harvesting of a flow-induced snapping sheet with nonuniform stiffness distribution

Zhaokun Wang ; Jingyu Cui ; Fuwang Zhao ; M. N. Mumtaz Qadri ; Yuanye Zhou ; Hui Tang

International Journal of Fluid Engineering 1, 043502 (2024)
https://doi.org/10.1063/5.0222003

International Journal of Fluid Engineering

RESEARCH ARTICLE

pubs.aip.org/hgmri/ijfe

Featured

Dynamics and energy harvesting of a flow-induced snapping sheet with nonuniform stiffness distribution

Cite as: Int. J. Fluid Eng. 1, 043502 (2024); doi: 10.1063/5.0222003
Submitted: 4 June 2024 • Accepted: 16 September 2024 •
Published Online: 16 October 2024

Zhaokun Wang,[1,2] Jingyu Cui,[3] Fuwang Zhao,[1,2,a)] M. N. Mumtaz Qadri,[4,a)] Yuanye Zhou,[5,a)] and Hui Tang[1]

AFFILIATIONS

[1] Department of Mechanical Engineering, The Hong Kong Polytechnic University, Kowloon, Hong Kong, China
[2] School of Fashion and Textiles, The Hong Kong Polytechnic University, Kowloon, Hong Kong, China
[3] Zhejiang Key Laboratory of Multiphase Flow and Fluid Machinery, Zhejiang Sci-Tech University, Hangzhou 310018, China
[4] Department of Aerospace Engineering, School of Mechanical and Manufacturing Engineering, NUST, Islamabad 44000, Pakistan
[5] Shenzhen Research Institute of Shandong University, A301 Virtual University Park in South District of Shenzhen, Shenzhen, China

[a)] **Authors to whom correspondence should be addressed:** f.w.zhao@connect.polyu.hk; mnmumtaz.qadri@smme.nust.edu.pk; and zhyy2009@163.com

ABSTRACT

Energy harvesting through periodic snap-through of a buckled sheet has recently gained considerable attention because of its potential applications in energy harvesting in low incoming flow. Although the snapping dynamics of uniform buckled sheets has been extensively studied, the present work focuses on the energy harvesting and dynamics of a nonuniform snapping sheet with both of its ends clamped in a channel flow. The analysis reveals that the sheet undergoes periodic snap-through oscillations, with its rear half consistently serving as the main contributor to effective energy harvesting, and the potential energy contributing significantly more than the kinetic energy. Varying the stiffness difference ΔEI^* shows that increasing the stiffness of the rear part and decreasing that of the fore part shifts the deformation wave toward upstream and enhances the snapping amplitude of the fore part, optimizing energy extraction. At a length compression ratio $\Delta L^* = 0.3$, the maximum potential energy is observed for $\Delta EI^* = 1$, and the total energy peaks at $\Delta EI^* = 2$. The study also identifies an optimal $\Delta L^* = 0.4$ that maximizes both total and potential energies, and triples the potential energy in comparison with $\Delta L^* = 0.1$. However, the enhancement of nonuniformity disappears at $\Delta L^* > 0.3$ for the total energy and $\Delta L^* > 0.2$ for the potential energy. These findings provide insights to aid optimization of the design and performance of snapping sheet energy harvesters.

I. INTRODUCTION

In recent decades, renewable energy sources derived from fluid flows, such as ocean and wind energy, have attracted considerable attention as approaches to address escalating environmental issues and the energy crisis.[1,2] Numerous devices such as wind and water turbines have been invented to harvest energy from the ambient environment.[3–6] Although these devices are efficient, they have several drawbacks, such as noise pollution, excessive land occupancy, costly manufacture, and high installation costs.[4–8] Energy harvesting by flow-induced vibration (FIV) has become more attractive recently and seems to be a viable solution. This approach leverages abundant environmental resources and offers notable environmental benefits, presenting a viable solution to overcome the constraints of conventional energy supplies.[9–13]

Various energy harvesters utilizing FIV have been developed to capture water and wind energy, such as the Vortex Induced

Vibration Aquatic Clean Energy (VIVACE) system, first introduced in 2008.[14,15] In VIVACE, an elastically supported cylinder vibrates along with vortex shedding, converting hydrokinetic energy into electrical energy. Many studies on VIV-based energy harvesters have highlighted their considerable efficiency in low-speed incoming flow, but have also noted their limitation of a narrow optimal velocity range.[14,16–22] One effective method to broaden the resonance range is to replace the linear spring with a nonlinear one, which can amplify the flapping amplitude by triggering the "snap-through" phenomenon, thus enhancing energy harvesting efficiency.[10,23–26] The phenomenon known as snap-through motion is typified by a rapid transition between equilibrium states in a bistable system, characterized by the conversion of kinetic and potential energies. Such snap-through motion substantially enhances energy harvesting efficiency, given the significant snapping amplitude activated by the pre-stored potential energy during snapping oscillations.[27] Moreover, snapping-based harvesters exhibit the capacity to oscillate steadily and periodically over a wider range of vibration frequencies, commencing from a low cut-in speed and overcoming the limited operating range of VIV. The underlying mechanisms of these harvesters have been extensively examined in Refs. 10, 16, and 28–34. Theoretical and numerical studies by Badhurshah *et al.*[10,30] demonstrated that incorporating a bistable spring into a VIV cylinder increases oscillation amplitude and broadens the reduced velocity range for operation. These findings are further validated by an equilibrium-constraint-based theory.[29] Recent developments have extended the scope of energy harvesting through flow-induced vibrations to include flapping flexible sheets activated by external forces such as vibrational forces[35] and microchannel flow.[36] Kim *et al.*[37] introduced triboelectric nanogenerators (TENGs) for small-scale wind energy harvesting, which outperformed previous systems in power generation and controllability. Further research into the stability of buckled sheets and their post-critical behavior in snapping motion has shown their potential for use in harvester arrays.[11] Gomez *et al.*[36] identified the critical flow velocity required to start snap-through in channel flows, and other studies have optimized snapping bistable sheets by modifying thickness, external excitation intensity, and boundary conditions.[38–41]

While previous studies have provided valuable insights into flexible snapping sheets, they have primarily focused on the dynamics of sheets with uniform stiffness distributions. However, natural structures like bird wings and fish fins often exhibit nonuniform properties, with variations in material characteristics and thickness along the chord.[42,43] These variations are essential for their effective function, implying that mimicking such nonuniformity could improve the performance of engineered systems. Recent studies have investigated and confirmed that the distribution of material properties can greatly enhance a flexible plate's propulsion and efficiency.[42–44] Despite this progress, the impact of nonuniform stiffness on energy harvesting enhancement remains inadequately explored. To the best of our knowledge, there has been a notable lack of studies to date on the energy-harvesting properties and dynamics of nonuniform sheets. The role of a nonuniform stiffness distribution in energy-harvesting capabilities and dynamics remains an open question. Understanding how the stiffness distribution affects the dynamics and energy properties of snapping plates could greatly benefit the development of more efficient energy harvesters. Future research on this topic could pave the way for the development of optimized snapping plate systems that harness energy more efficiently and adapt more effectively.

This study aims to address the existing research gap by developing an innovative fluid–structure interaction (FSI) model that accurately captures the dynamics of a snapping sheet. We perform an in-depth examination of the snapping dynamics pertaining to a buckled sheet featuring various stiffness patterns, aiming to deepen knowledge of a precompressed sheet's dynamics, thereby providing insights into the optimization of snap-through-based energy harvesters. The remainder of this paper is organized as follows. Section II describe the physical problem and the methodology used. Section III details and discusses the results. Finally, several pertinent conclusions are given in Sec. IV.

II. PROBLEM STATEMENT AND METHOD

A. Problem description

We investigate a fluid–structure system as depicted in Fig. 1. A flexible plate is considered to model the two-dimensional elastic sheet, embedded in a channel flow, with a parabolic inflow velocity. The maximum streamwise velocity U is at the center of the channel. The sheet is characterized by its line density ρ_s, chord length L, and bending and stretching stiffnesses EI and EA. Notably, the stiffnesses EI and EA can be adjusted along the sheet, with the EI distribution patterns shown in Fig. 2. The surrounding fluid is characterized by its kinematic viscosity ν and density ρ_f. With both edges clamped parallel to the incoming free flow, the sheet is first compressed by $\Delta L = L - L_0$ through advancing the rear edge toward the upstream direction to initiate the snapping motion. Additional details of the configuration are provided in the schematic in Fig. 1(a).

The dynamics of the fluid flow is governed by the incompressible Navier–Stokes equations

$$\nabla \cdot \boldsymbol{u} = 0, \tag{1}$$

$$\frac{\partial \boldsymbol{u}}{\partial t} + \boldsymbol{u} \cdot \nabla \boldsymbol{u} = -\frac{1}{\rho_f}\nabla p + \nu \nabla^2 \boldsymbol{u} + \boldsymbol{f}_e, \tag{2}$$

where $\boldsymbol{u}$ denotes the fluid velocity, ρ_f the density of the fluid, ν the kinematic viscosity, p the pressure, and $\boldsymbol{f}_e$ the external body force taking account of the presence of the structure.

The large-scale motion and deformation of the sheet are governed by the following structural equation:[45,46]

$$\rho_s \frac{\partial^2 \boldsymbol{X}}{\partial t^2} = \frac{\partial}{\partial s}\left[EA\left[1 - \left(\frac{\partial \boldsymbol{X}}{\partial s}\cdot\frac{\partial \boldsymbol{X}}{\partial s}\right)^{-1/2}\right]\frac{\partial \boldsymbol{X}}{\partial s} - \frac{\partial}{\partial s}\left(EI\frac{\partial^2 \boldsymbol{X}}{\partial s^2}\right)\right] + \boldsymbol{F}_f, \tag{3}$$

where X denotes the sheet's position vector. Its bending stiffness is denoted by EI and its stretching stiffness by EA. F_f denotes the fluid force acting on the surface of the sheet and ρ_s the line density. s denotes the Lagrangian coordinate along the sheet. The nondimensionalized governing equations are detailed in our previous study,[40] with a comprehensive definition of the nondimensional parameters being provided in Refs. 39 and 40.

In the simulation, the flow fluid is first initialized into a completely developed velocity field with a parabolic distribution in the transverse direction. Simultaneously, the sheet is precompressed by

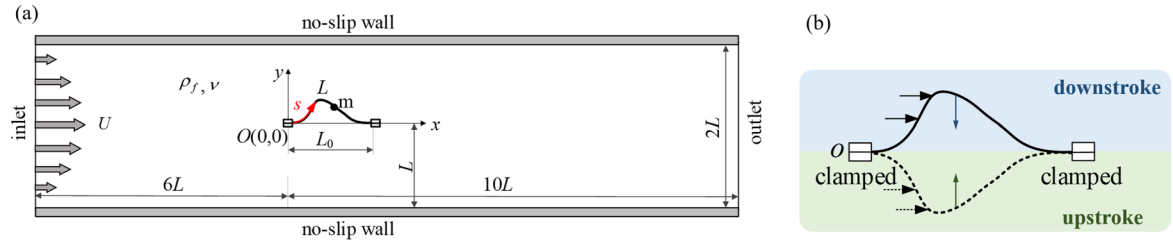

FIG. 1. (a) Two-dimensional schematic of elastic sheet in channel flow. The sheet has length L and an initial precompressed distance L_0 between its front and rear ends. The front edge is located at the origin point O. (b) Switching between downstroke and upstroke for the snap-through sheet.

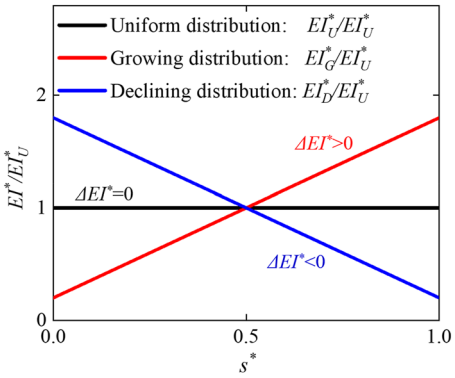

FIG. 2. Stiffness distribution patterns along the sheet: a uniform distribution ($\Delta EI^* = 0$), a growing distribution ($\Delta EI^* > 0$), and a declining distribution ($\Delta EI^* < 0$).

ΔL and develops into a buckled state (see Fig. 1). No-penetration and no-slip conditions are applied to the sheet's surfaces, as well as the flow domain's top and bottom boundaries. At both edges of the sheet, a clamped boundary condition is enforced. At the upstream inlet, a parabolic velocity is applied, while the downstream outlet is subjected to a constant-pressure boundary condition.

For the nondimensionalization of the governing parameters, the characteristic density ρ_f, sheet length L, and velocity U are selected, giving

$$\mathrm{Re} = \frac{UL}{\nu}, \quad EI^* = \frac{EI}{\rho U^2 L^3}, \quad EA^* = \frac{EA}{\rho U^2 L}, \quad m^* = \frac{\rho_s}{\rho_f L}, \quad \Delta L^* = \frac{\Delta L}{L}, \tag{4}$$

where Re denotes the Reynolds number, EI^* the bending stiffness, EA^* the stretching stiffness, m^* the sheet's mass ratio, and ΔL^* the compression ratio of the sheet.

In our structural model, the sheet is divided into multiple elements or segments along its chord. To account for the nonuniform stiffness distribution, each element is assigned a unique constant. Here, we consider three types of stiffness distribution: a uniform distribution EI_U^*, a declining distribution EI_D^*, and a growing distribution EI_G^*, all having the same arithmetic mean stiffness. These linear distributions can be characterized using a unified parameter ΔEI^*, which quantifies the stiffness variation between the rear and front ends of the sheet. Specifically, $\Delta EI^* = 0$ signifies a uniform distribution, $\Delta EI^* > 0$ a growing distribution, and $\Delta EI^* < 0$ a declining distribution.

To assess the energy characteristics of the snapping sheet, energy coefficients for the instantaneous kinetic energy E_k^* and potential energy E_p^*, along with their distributed counterparts E_{dk}^* and E_{dk}^*, are defined as follows:

$$E_k^* = \frac{E_k}{0.5\rho_f L^2 U^2}, \quad E_p^* = \frac{E_p}{0.5\rho_f L^2 U^2}, \quad E_{dk}^* = \frac{E_{dk}}{0.5\rho_f L U^2}, \quad E_{dp}^* = \frac{E_{dp}}{0.5\rho_f L U^2}, \tag{5}$$

where $E_k = 0.5\rho_s \int_0^L (\partial \boldsymbol{X}/\partial t)^2 ds$ is the kinetic energy and $E_p = 0.5EI \int_0^L \left(\partial^2 \boldsymbol{X}/\partial s^2\right)^2 ds$ is the potential energy. The sum of the potential and kinetic components is the total energy coefficient, defined as $E^* = E_p^* + E_k^*$. The energy densities for the potential and kinetic components along the sheet are given by $E_{dp} = 0.5EI\left(\partial^2 \boldsymbol{X}/\partial s^2\right)^2$ and $E_{dk} = 0.5\rho_s(\partial \boldsymbol{X}/\partial t)^2$, respectively. $E_d^* = E_{dk}^* + E_{dp}^*$ is the coefficient of total energy density.

The energy harvesting efficiency can be evaluated by the following time-averaged energy coefficients:

$$\bar{E}_k^* = \frac{\bar{E}_k}{0.5\rho_f L^2 U^2}, \quad \bar{E}_p^* = \frac{\bar{E}_p}{0.5\rho_f L^2 U^2}, \quad \bar{E}_{dk}^* = \frac{\bar{E}_{dk}}{0.5\rho_f L U^2}, \quad \bar{E}_{dp}^* = \frac{\bar{E}_{dp}}{0.5\rho_f L U^2}, \tag{6}$$

where

$$\bar{E}_k = 0.5\rho_S \int_t^{t+T_f} \int_0^L \left(\frac{\partial \boldsymbol{X}}{\partial t}\right)^2 ds dt/T_f, \quad \bar{E}_p = 0.5EI \int_t^{t+T_f} \int_0^L \left(\frac{\partial^2 \boldsymbol{X}}{\partial s^2}\right)^2 ds dt/T_f, \tag{7}$$

with T_f being the oscillation period of the snapping sheet. The overall energy-harvesting efficiency is $\bar{E}^* = \bar{E}_p^* + \bar{E}_k^*$. The time-averaged potential and kinetic energy densities are defined as

$$\bar{E}_{dp} = 0.5T_f EI \int_t^{t+T_f} \left(\frac{\partial^2 \boldsymbol{X}}{\partial s^2}\right)^2 dt, \quad \bar{E}_{dk} = 0.5T_f \rho_s \int_t^{t+T_f} \left(\frac{\partial \boldsymbol{X}}{\partial t}\right)^2 dt. \tag{8}$$

The total time-averaged density coefficient is given by $\overline{E}_d^* = \overline{E}_{dk}^* + \overline{E}_{dp}^*$.

B. Numerical method

The lattice Boltzmann method (LBM) is employed for simulating the fluid flow because of its time-efficiency and suitability for parallel computing.[47–50] The multiple-relaxation-time lattice Boltzmann equation (MRT-LBE) with external force scheme[49,51–53] is adopted to enhance stability, with the evolution equation given by

$$f_\alpha(\boldsymbol{x}+\boldsymbol{c}_\alpha\Delta t, t+\Delta t) - f_\alpha(\boldsymbol{x},t) = -\boldsymbol{M}^{-1}S\boldsymbol{M}\left[f_\alpha(\boldsymbol{x},t) - f_\alpha^{eq}(\boldsymbol{x},t)\right] - \boldsymbol{M}^{-1}\left(\boldsymbol{I}-\frac{\boldsymbol{S}}{2}\right)\boldsymbol{M}g_\alpha(\boldsymbol{x},t)\Delta t, \quad (9)$$

where $f_\alpha(x, t)$ are the particle distribution functions. The collision operator is represented by the first term on the right-hand side of Eq. (7), with S being the relaxation matrix and M the transformation matrix. The equilibrium distribution function f_α^{eq} is defined as

$$f_\alpha^{eq} = w_\alpha\left[\rho_f + \rho_{f0}\left(\frac{\boldsymbol{c}_\alpha\cdot\boldsymbol{u}}{c_s^2} + \frac{(\boldsymbol{c}_\alpha\cdot\boldsymbol{u})^2}{2c_s^4} - \frac{\boldsymbol{u}^2}{2c_s^2}\right)\right], \quad (10)$$

where c_s denotes the sound speed, ρ_{f0} the mean mass density, and w_α a weighting coefficient. The approach to modeling the effect of the immersed body on the fluid employs the force scheme suggested by Guo *et al.*[51] In the computation, the fluid density ρ_f and velocity $\boldsymbol{u}$ are evaluated by

$$\rho_f = \sum_\alpha f_\alpha, \boldsymbol{u} = \sum_\alpha \boldsymbol{c}_\alpha f_\alpha + \frac{\Delta t}{2}\boldsymbol{f}_e. \quad (11)$$

The dynamics of the snapping sheet are examined using the finite element method. The co-rotational scheme[54–57] is chosen to address the severe deformation observed in the snapping sheet. This scheme separates the large elemental motion into a large rigid movement and a minor pure deformation. Thus, problems related to severe geometrical nonlinearity are resolved through the coordinate transformation between the local co-rotational coordinate and the global one. Additional details of this numerical methodology are available in Refs. 39, 40, 50, 58, and 59.

The fluid–structure interaction is tackled by employing the direct-forcing immersed boundary method (IBM).[49,60] The force density exerted at the interface between the fluid and the structure is estimated by the formula

$$\boldsymbol{F}_f(s,t) = -2\rho_f\frac{\boldsymbol{U}(s,t)-\boldsymbol{u}(s,t)}{\Delta t}, \quad (12)$$

where U, defined as $U = \partial X/\partial t$, denotes the velocity of the structure boundary, and $\boldsymbol{u}$ denotes the fluid velocity at the sheet's boundary position. The fluid velocity u is determined by interpolating over the fluid domain Ω using the expression

$$\boldsymbol{u}(\boldsymbol{s},t) = \int_\Omega \boldsymbol{u}(\boldsymbol{x},t)\delta(\boldsymbol{x}-\boldsymbol{X}(\boldsymbol{s},t))dx, \quad (13)$$

where δ is the Dirac delta function.[49] The interaction force $\boldsymbol{F}_f$ is subsequently spread onto the adjacent fluid through the formula

$$\boldsymbol{f}_e(\boldsymbol{x},t) = -\int_\Gamma \boldsymbol{F}_f(s,t)\delta(\boldsymbol{x}-\boldsymbol{X}(s,t))ds, \quad (14)$$

which enforces the no-penetration and no-slip conditions on the sheet's surface.

C. Numerical verification

To validate the accuracy of the structural solver, we conducted simulations of the buckled sheet's equilibrium state and compared them with those derived from nonlinear elasticity theory,[61] as well as experimental observations.[62] The sheet, clamped at both ends, was deformed by a precompression ΔL^*. Figure 3(a) shows a comparison of the buckled state at $\Delta L^* = 0.5$ between the present results, theoretical predictions, and experimental solutions. The good agreement across all comparisons affirms the model's accuracy in handling extreme structural deformation. The consistency in transverse displacements between our numerical solver, experiment, and elasticity theory depicted in Fig. 3(b) further supports this. Additional details of the solver's verification for severe geometric nonlinearity are provided in Ref. 59.

To verify the numerical method used in the present fluid–structure interaction study, the flow across a two-dimensional flapping flag was simulated.[63] The key governing parameters were Re = 200, $EI^* = 0.0015$, $m^* = 1.5$, Froude number $Fr = 1.414$, and $EA^* = 2500$, identical to those in Ref. 63. The y-direction displacement of the plate's trailing edge is illustrated in Fig. 4(a), from which it can be seen that the current results are in good agreement with those of Lee and Choi.[63] To guarantee the independence of the outcome on selected grid and time steps, we conducted a convergence study using various grid sizes and time steps, as detailed in Fig. 4(b). The minor discrepancies in the y-direction displacement at the sheet's central point indicate convergence, allowing us to select a grid spacing of $\Delta x = L/80$ and a time step of $\Delta t = L/4000u$ for an optimal balance of accuracy and computational efficiency.

III. RESULTS AND DISCUSSION

This study primarily explores the influences of the stiffness distribution on a snapping sheet's dynamics and energy characteristics. Unless stated otherwise, the default parameters for our simulations are Re = 200, $\Delta L^* = 0.3$, and $EI^* = 0.002$ for the uniform stiffness case. Furthermore, to eliminate the tensibility of the sheet, the stretching stiffness is chosen as $EA^* = 1000$, and the mass ratio is maintained at $m^* = 1.0$.

A. Dynamics and energy characteristics of uniform sheet

To explore the sheet's dynamics, we examine the propagation of a deformation wave in the selected uniform case at $\Delta L^* = 0.3$, $EI^* = 0.001$, and $m^* = 1$. In Fig. 5, the periodic snapping is illustrated in superimposed sequential profiles. Two distinct sheet movements are specifically observed in the sequential process: a streamwise shift [see Figs. 5(a1)–5(a3)] and an up-to-down snapping motion [see Figs. 5(a4)–5(b4)]. In the streamwise shift, the sheet's deformation wave moves from upstream to downstream, while in the up–down snapping motion, the sheet snaps from the downside (upside) to the upside (downside). At moment T_1 ($t/T_f = 0.10$), corresponding to the moment of point 1 in Fig. 6, an "S" form develops, with the sheet's rear part snapping up. Subsequently, the snapping motion initiates a sudden notable transformation of potential

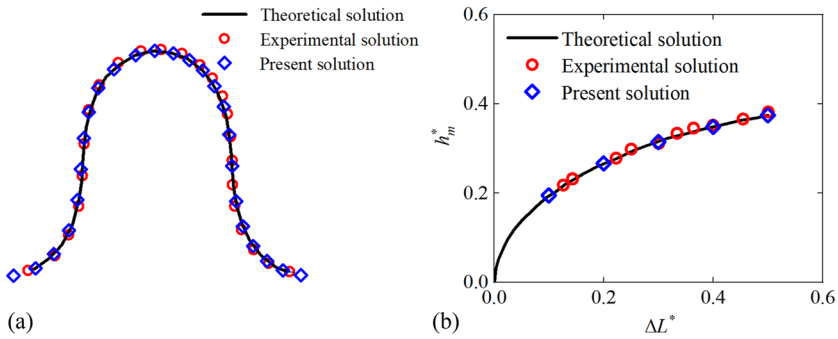

FIG. 3. (a) The sheet's initial buckled shapes at $\Delta L^* = 0.5$ and (b) Comparison of the transverse displacement h_m^* of the sheet's middle point between our results (blue diamonds), experimental measurements[62] (red circles), and theoretical solution[61,62] (black line).

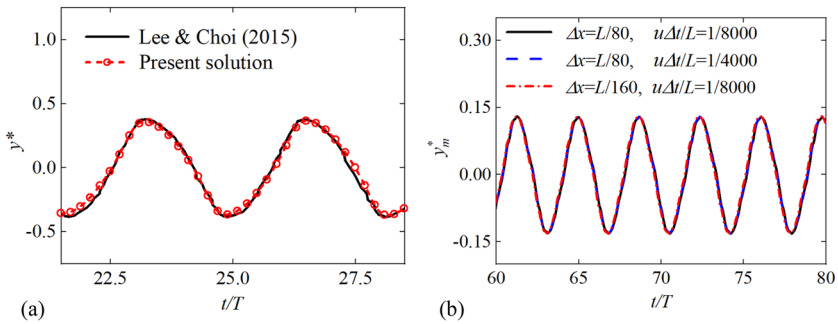

FIG. 4. (a) Evolution of y-direction displacement at the trailing edge of the plate for Re = 200, $EI^* = 0.0015$, $EA^* = 2500$, $m^* = 1.5$, and $Fr = 1.414$; (b) Instantaneous y-direction displacement of the sheet's midpoint y_m^* at different grid and time steps, where Re = 200, $EI^* = 0.0005$, $m^* = 1.0$, $\Delta L^* = 0.2$, and $EA^* = 1000$.

energy into kinetic energy, which results in the kinetic energy attaining its maximum and the potential energy reaching its minimum simultaneously at $t/T_f = 0.15$; see Fig. 5(a2) and point 2 in Fig. 6. Following this, the sheet's deformation wave formed after snap-through [see Fig. 5(a2)] propagates streamwise, producing a pronounced curvature at the sheet's rear part, as illustrated in Fig. 5(a3). Consequently, this leads to a significant augmentation in potential energy, reaching a peak value at $t/T_f = 0.27$ (point 3 in Fig. 6), while the kinetic energy reaches its minimum value. Subsequently, the potential energy stored in the sheet is rapidly released [see Fig. 5(a4)],

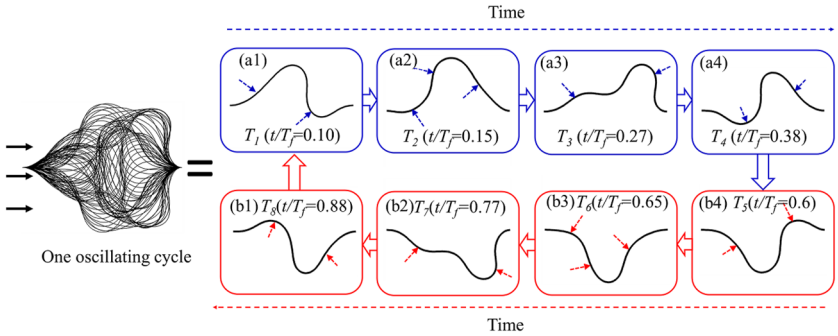

FIG. 5. Superimposed snapshots of the snapping sheet in one period of oscillation, demonstrating the propagation of the sheet's deformation wave at Re = 200, $EI^* = 0.002$, $\Delta L^* = 0.3$, and $m^* = 1.0$. On the left are the enveloping lines of the sheet throughout a single snap-through period. On the right, the sheet's motion is decomposed to illustrate its wave propagation process. The times with the maximum total energy, minimum potential energy, maximum potential energy, and minimum total energy are represented by the time occurrences $T_1(T_5)$, $T_2(T_6)$, $T_3(T_7)$, and $T_4(T_8)$, respectively. These time instants correspond to the points 1–4 defined in Fig. 6. Their temporal values are assigned in relation to the instant at which the midpoint of the sheet traverses the midline in downside-to-upside motion.

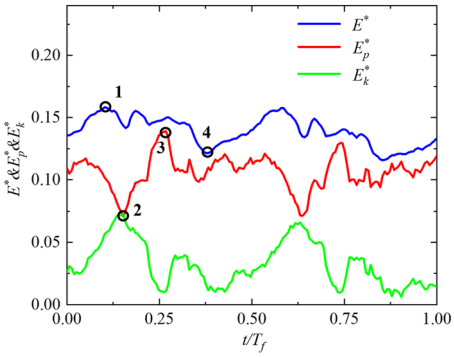

FIG. 6. Time evolutions of the total E^* (blue line), potential E_p^* (red line), and kinetic E_k^* (green line) energies in a representative cycle for the scenario with Re = 200, $\Delta L^* = 0.3$, $EI^* = 0.002$, and $m^* = 1$. The time t is assigned relative to the instant at which the sheet's midpoint crosses the midline from downside to upside, and it is scaled by the snapping cycle T_f. Some typical instants with the largest $\overline{E}^*$, E_k^*, or E_p^* are marked with hollow black circles.

which is accompanied by the total energy reaching its minimum (point 4 in Fig. 6). The sheet then undergoes a downside-to-upside motion, triggering a comparable snapping dynamic as the preceding upside-to-downside motion.

To gain insight into the sheet's energy characteristics and dynamics, we further examine the instantaneous pressure field, vortex evolution (see supplementary material), interaction force, and velocity distributions along the snapping sheet at selected time instances (see Fig. 7). At $t/T_f = 0.10$, the maximum E^* is obtained (see point 1 in Fig. 6), which can be attributed to both the relatively high velocity distributed and the considerable curvature present along the sheet, as depicted in Figs. 7(a1)–7(d1). The considerable pressure disparity across the sheet, significantly driven by the negative single vortex induced by the snapping motion (V_{snap}), results in a downward force on the sheet's fore surface and an upward force on its rear surface. This force distribution leads to the sheet's rear part snapping upside, shifting the deformation wave downstream [see Figs. 5(a1) and 7(d1)], while simultaneously releasing the stored potential energy in the sheet's rear portions. As the snapping vortex V_{snap} further evolves and prepares to shed, the potential energy E_p^* reaches its minimum at $t/T_f = 0.15$, coinciding with the largest E_k^* (see Fig. 6), where the considerable upward velocity concentrated in the sheet's rear section largely contributes the peak E_k^*, as illustrated in Figs. 5(a2) and 7(d2). Following this, a pair of vortices (V_p) emerges: a positive vortex forms behind the sheet, and a negative vortex appears on the upper surface of the sheet's rear section [see Fig. 7(b3)]. The increased pressure difference resulting from these vortices generates a streamwise force component on the sheet, further propagating the deformation wave in the downstream direction [see Figs. 7(a3) and 7(c3)]. By $t/T_f = 0.27$, significant deformation in the rear part of the sheet leads to the generation of substantial potential energy (point 3 in Fig. 6). By contrast, the kinetic energy E_k^* decreases to its minimum, which is further corroborated by the negligible distribution of velocity observed along the sheet, as shown in Fig. 7(d3). Subsequently, at $t/T_f = 0.38$, a positive V_{snap} forms beneath the sheet, following the vortex V_p shedding. The low pressure induced by this positive V_{snap} substantially contributes to the downward force acting on the sheet, driving it to snap downward, as depicted in Figs. 5(a2) and 7(c4), thus initiating the upside-to-downside snap-through.

To delve deeper into the energy contributions of the sheet's different segments, the energy densities distributed along the sheet throughout a single steady snap-through motion have been assessed and are depicted in Fig. 8. These results suggest that the potential energy E_{dp}^* predominates over the kinetic energy E_{dk}^* in contributing to the total energy E_d^*, as illustrated in Figs. 8(a)–8(c). This is further supported by time-averaged energy densities in Fig. 8(d). For the elastic bending energy, the rear part of the sheet, specifically $s^* = 0.5$–1.0 [see Fig. 8(b)], contributes the majority of the potential energy harvesting. Two prominent intensity bands are observed at $s^* = 0.7$ and 1.0, corresponding to the two peaks of potential energy $\overline{E}_{dp}^*$, as shown in Fig. 8(d). Regarding the kinetic energy E_{dk}^*, Fig. 8(d) indicates that the majority of the kinetic energy is derived from the section $s^* = 0.5$–0.75. Given that the potential energy contributes much more than the kinetic energy, a similar distribution pattern is observed between the time-averaged total ($\overline{E}_d^*$) and potential ($\overline{E}_{dp}^*$) energies, as illustrated in Fig. 8(d). Given that the concentration of both kinetic and potential energies occurs in the sheet's latter half

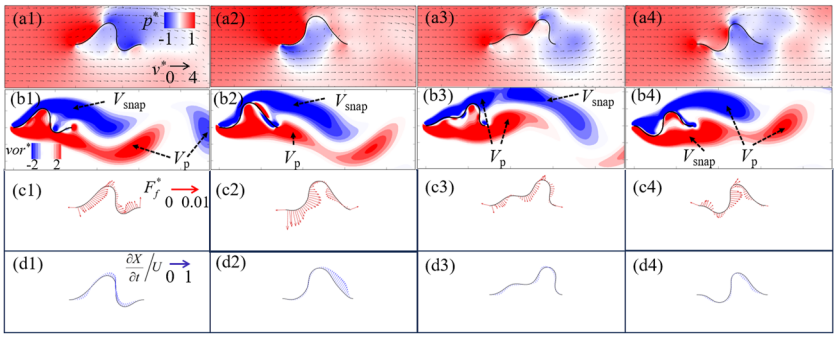

FIG. 7. (a) Instantaneous pressure field around the sheet together with flow arrows, (b) vortex evolution (see supplementary material), (c) interaction force, and (d) velocity distributions along the snapping sheet at selected time instants. The four instances (marked as "1," "2," "3," and "4") line up with the hollow circles that are marked at $t/T_f = 0.10$, 0.15, 0.27, and 0.38 in Fig. 6.

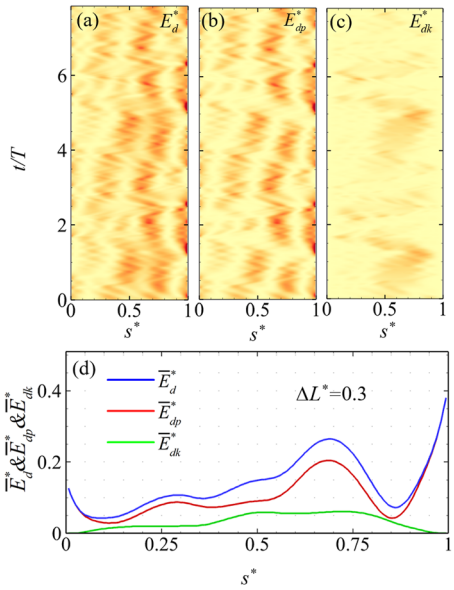

FIG. 8. (a)–(c) Temporal distributions of total energy density E_d^*, potential energy density E_{dp}^*, and kinetic energy density E_{dk}^*, respectively, across the snapping sheet. (d) Mean energy densities over one characteristic snapping cycle, where the blue line represents the total energy $\overline{E}_d^*$, the red line the potential energy $\overline{E}_{dp}^*$, and the green line the kinetic energy $\overline{E}_{dk}^*$.

section, the sheet's rear section accumulates a much larger share of the energy than the front segment.

B. Effect of ΔEI^*

The effect of ΔEI^* on the sheet's energy-harvesting properties and dynamics are further explored in this subsection. Figure 9 presents the equilibrium forms of the buckled sheet in the absence of fluid forces (first row) and the corresponding enveloping lines in one typical cycle (second row) with different ΔEI^*. The initial shapes show that ΔEI^* significantly affects the initial deformation of the sheet. As ΔEI^* increases from −3.9 to 3.9, the deformation wave shifts noticeably from downstream toward upstream (see the first row of Fig. 9). In addition, the variation of ΔEI^* largely alters

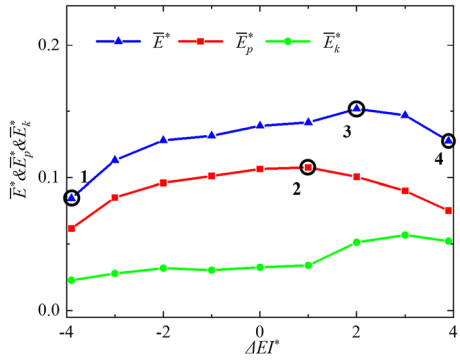

FIG. 10. Effect of ΔEI^* on mean total ($\overline{E}^*$), potential ($\overline{E}_p^*$), and kinetic ($\overline{E}_k^*$) energies at $\Delta L^* = 0.3$. Hollow black circles mark specific moments when the largest values of $\overline{E}^*$, E_k^*, or E_p^* are observed.

the oscillating patterns of the sheet, as shown in the second row of Fig. 9. When the sheet's rear part is softened and the fore part stiffened ($\Delta EI^* < 0$), the deformation of the rear part is significantly enhanced, while that of the fore part is suppressed [see Figs. 9(a2) and 9(b2)]. With increasing ΔEI^*, the fore part of the sheet becomes softened, while its rear part is stiffened. Consequently, the snapping amplitude of the fore part is strengthened, and that of the rear part is reduced, as illustrated in Figs. 9(d2) and 9(e2). It is also noteworthy that all scenarios featuring different ΔEI^* exhibit symmetrical snapping oscillations.

We further investigate the effect of ΔEI^* on the performance of energy extraction, as depicted in Fig. 10. It can be seen that the potential energy $\overline{E}_p^*$ initially exhibits an increase with increasing ΔEI^*, reaching a maximum at $\Delta EI^* = 1$, before subsequently decreasing. At $\Delta EI^* = 1$, two notable peaks exist at $s^* = 0.65$ and 1.0, along with a plateau exhibiting relatively high potential energy density between $s^* = 0.25$ and 0.5, contributing to the peak potential energy, as illustrated in Fig. 11(b). The total energy follows a similar trend, except that the peak occurs at $\Delta EI^* = 2$ (see Fig. 10). Compared with the case $\Delta EI^* = 1$, the potential energy $\overline{E}_p^*$ decreases slightly, but the kinetic energy $\overline{E}_k^*$ increases significantly, resulting in an increase in the total energy $\overline{E}^*$. This observation is corroborated by the energy density in Fig. 11(c), which highlights an increase in kinetic energy amplitude alongside a decrease

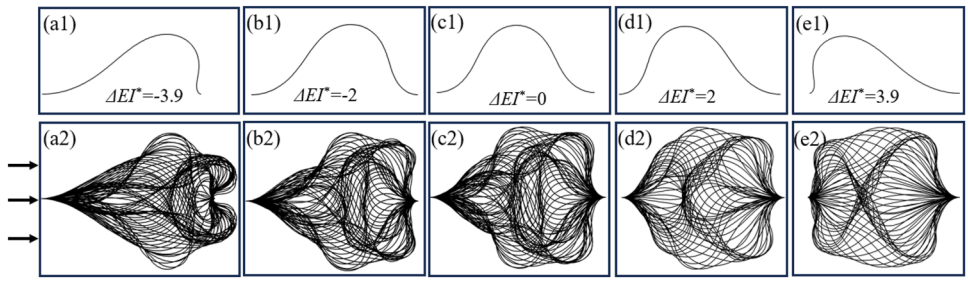

FIG. 9. Initial equilibrium forms of the buckled sheet in the absence of fluid forces (first row) and superimposed snapshots of the snapping sheet through one oscillating cycle (second row) at $\Delta L^* = 0.3$ for $\Delta EI^* = -3.9$ (a), −2 (b), 0 (c), 2 (d), and 3.9 (e).

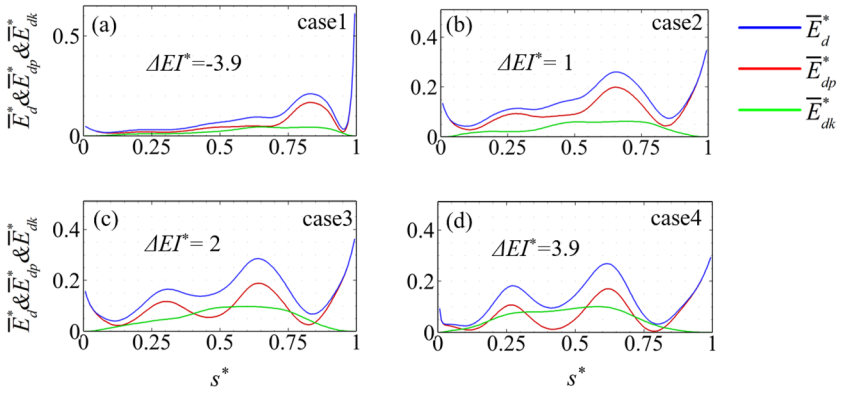

FIG. 11. Mean total ($\overline{E}^*_d$), potential ($\overline{E}^*_{dp}$), and kinetic ($\overline{E}^*_{dk}$) energy densities along the snapping sheet at $\Delta L^* = 0.3$. (a)–(d) (cases 1–4) correspond to the points 1–4 marked in Fig. 10.

in potential energy density, particularly at $s^* \approx 0.45$, when compared with the $\Delta EI^* = 1$ scenario [see Fig. 11(b)]. In terms of kinetic energy, a significant increase is noted when ΔEI^* reaches 1.0, following an initial large plateau, after which it maintains a relatively high value, as shown in Fig. 10. A comparative analysis of the $\Delta EI^* = -3.9$ and 3.9 cases reveals that the $\Delta EI^* = 3.9$ configuration (with a stiffer rear and a softer fore section) outperforms the $\Delta EI^* = -3.9$ configuration in both potential and kinetic metrics, as can be seen from Figs. 11(a) and 11(d) and points 1 and 4 in Fig. 10.

Figure 12 shows the variation of the flapping period $T_f{}^*$ of the snapping sheet as a function of ΔEI^*, together with the corresponding instantaneous vorticity contours, at $\Delta L^* = 0.3$. As can be seen from Fig. 12(a), the flapping period decreases markedly with an increase in ΔEI^*. This indicates that when the stiffness is higher in the front part of the sheet and lower in the rear part, the sheet's oscillation frequency decreases; conversely, when the stiffness is higher in the rear part and lower in the front part, the sheet oscillates with a higher frequency. This behavior aligns with the variation in kinetic energy E_k^* observed in Fig. 10, where an increase in ΔEI^* corresponds to a rise in kinetic energy. Figure 12(b) presents the instantaneous vorticity contours for various values of ΔEI^* (see supplementary material). Despite differences in ΔEI^*, a similar wake pattern of 2P + 2S, comprising two pairs of V_p vortices and two V_{snap} vortices, is observed throughout the snapping cycle. In some cases, namely, when $\Delta EI^* = -3.9$, -2, and 0, the V_{snap} vortex may split into two parts, but the overall vortex pattern remains consistent. As ΔEI^* increases, the spacing between vortices decreases, indicating a higher oscillation frequency. Simultaneously, the vortex strength increases, suggesting a stronger interaction between the sheet and the fluid. This enhanced interaction increases the harvested energy. When combined with the contribution of kinetic energy E_k^* and the effect of nonuniform stiffness, the overall energy reaches its peak at $\Delta EI^* = 1.0$.

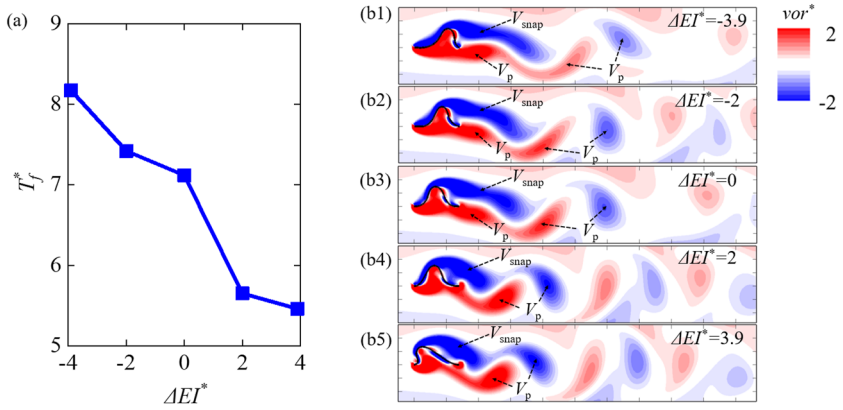

FIG. 12. (a) Flapping period of snapping sheet, $T_f{}^*$, defined as $T_f U/L$. (b) Instantaneous vorticity contours for sheet with $\Delta L^* = 0.3$ at $\Delta EI^* = -3.9$, -2, 0, 2, and 3.9 (see supplementary material).

C. Effect of ΔL^*

As previously discussed, $\Delta EI^* = 2$ maximizes the total energy $\overline{E}^*$ at $\Delta L^* = 0.3$. However, previous studies[38–41] have suggested that the effectiveness of energy harvesting is closely connected to the precompression of the sheet, ΔL^*. To further explore the effect of ΔL^*, the time-averaged energies generated at various values of ΔL^* are presented for $\Delta EI^* = -2$, 0, and 2 for comparison in Fig. 13. It is observed that as ΔL^* increases, all the energy parameters initially increase and then decrease. Specifically, the potential energy $\overline{E}_p^*$ nearly triples for all ΔEI^* values at $\Delta L^* = 0.4$ compared with $\Delta L^* = 0.1$. (This enhancement is also evidenced by the energy density distribution shown in Fig. 15, where the potential energy is notably increased.) As ΔL^* increases to 0.5, $\overline{E}_p^*$ experiences a slight reduction. The kinetic energy $\overline{E}_k^*$ peaks at $\Delta L^* = 0.3$, decreases as ΔL^* deviates from 0.3, and becomes zero when $\Delta L^* = 0.5$. This zero kinetic energy indicates the absence of snapping motion, with the sheet transitioning into a steady state, as depicted in Fig. 14, where no periodic snap-through is observed. As for the effect of ΔEI^*, when $\Delta L^* < 0.3$, the stiffness pattern of $\Delta EI^* = 2$ increases the total energy, while $\Delta EI^* = -2$ suppresses total energy extraction. At $\Delta L^* = 0.4$ and 0.5, however, both $\Delta EI^* = -2$ and 2 decrease the energy harvesting. For example, at $\Delta L^* = 0.4$, compared with the uniform stiffness case with $\Delta EI^* = 0$ [see Fig. 15(a)], the harvested potential energy is weakened at the fore part for $\Delta EI^* = -2$ [see Fig. 15(b)] and the at the rear part for $\Delta EI^* = 2$ [see Fig. 15(c)]. With regard to the potential energy $\overline{E}_p^*$, the enhancement of energy harvesting at $\Delta EI^* = 2$ is effective when $\Delta L^* < 0.2$. This supports the discussion in Sec. II, indicating that the occurrence of the maximum total energy $\overline{E}^*$ at $\Delta L^* = 0.3$ (see point 3 in Fig. 10) is mainly due to the significant increase in kinetic energy $\overline{E}_k^*$, as depicted in Fig. 13.

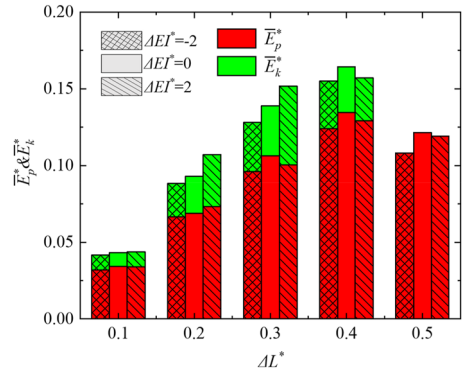

FIG. 13. Stacked bar graphs grouped together illustrating the relative proportions of the mean total ($\overline{E}^*$), potential ($\overline{E}_p^*$), and kinetic ($\overline{E}_k^*$) energies for cases with $\Delta L^* = 0.1$ (first group), 0.2 (second group), 0.3 (third group), 0.4 (fourth group), and 0.5 (fifth group). In each group, three cases are included, with the first column for $\Delta EI^* = -2$, the second $\Delta EI^* = 0$, and the third $\Delta EI^* = 2$. The red color represents the potential energy, and the green color the kinetic energy.

Figure 16 shows the instantaneous vorticity contours of the snapping sheet at various values of ΔL^*. As ΔL^* increases, the strength of the vortices intensifies. At $\Delta L^* = 0.1$ and 0.2, the wake

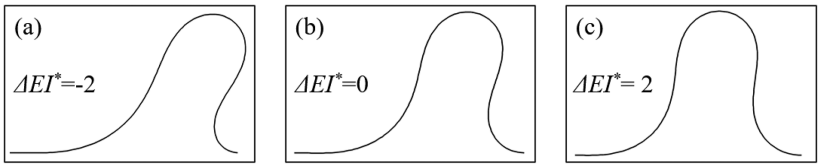

FIG. 14. Equilibrium shape of the sheet at $\Delta L^* = 0.5$ for $\Delta EI^* = -2$ (a), 0 (b), and 2 (c) in channel flow.

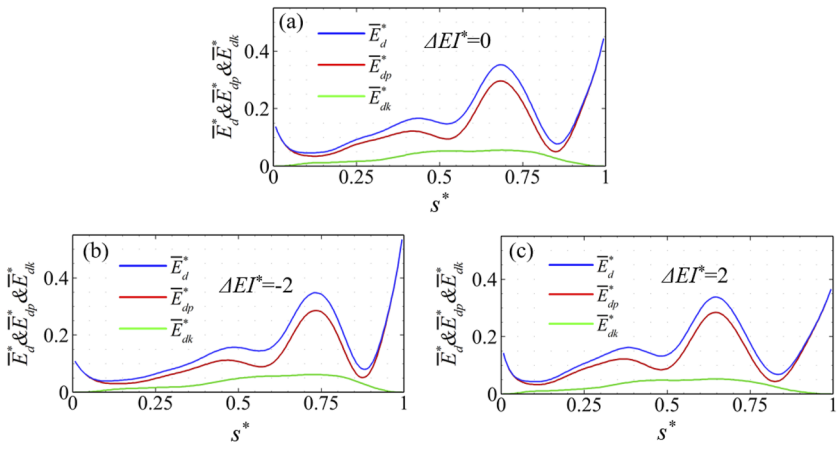

FIG. 15. Mean total ($\overline{E}_d^*$), potential ($\overline{E}_{dp}^*$), and kinetic ($\overline{E}_{dk}^*$) energies along the snapping sheet at $\Delta L^* = 0.4$. (a)–(c) correspond to $\Delta EI^* = 0$, −2, and 2, respectively, in Fig. 10.

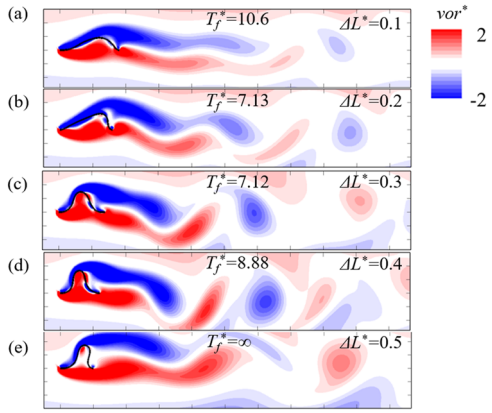

FIG. 16. Instantaneous vorticity contours for the sheet at $\Delta L^* = 0.1$ (a), 0.2 (b), 0.3 (c), 0.4 (d), and 0.5 (e) with $\Delta EI^* = 0$.

pattern is characterized by long shear layers, while beyond $\Delta L^* = 0.3$, the vortices become more distinct. The enhanced vortex structures signify stronger interaction between the sheet and the surrounding fluid, effectively increasing the potential energy. This observation is consistent with the energy distributions shown in Fig. 13, except for the case of $\Delta L^* = 0.5$, where no snap-through occurs. Additionally, at $\Delta L^* = 0.3$, the sheet exhibits the shortest oscillation period, indicating the fastest snapping and the highest kinetic energy, as is also evidenced by the kinetic energy data in Fig. 13. When both kinetic and potential energy contributions are considered, the total energy peaks at $\Delta L^* = 0.4$, as illustrated in Fig. 13.

IV. CONCLUSION

This study has numerically investigated the dynamics of a snapping sheet subjected to a laminar channel flow, employing a fluid–structure interaction model. We have analyzed the effects of the stiffness distribution on the energy-harvesting properties and the dynamics of the sheet. The key findings can be summarized as follows:

1. The energy characteristics and dynamics of a uniform snapping sheet have been examined under the conditions Re = 200, $\Delta L^* = 0.3$, $EI^* = 0.002$, and $m^* = 1.0$. The sheet undergoes periodic snap-through oscillations, oscillating from side to side periodically and continuously generating both potential and kinetic energies. Notably, the potential energy makes a much greater contribution than the kinetic energy. Furthermore, the rear half of the sheet consistently serves as the main contributor for effective energy harvesting, highlighting its critical role in energy harvesting.
2. The parameter ΔEI^*, which quantifies the stiffness variation between the rear and front parts of the sheet, has a clear influence on the sheet's initial buckled shape and snapping dynamics, but it does not affect the symmetry of the snapping mode. Increasing ΔEI^* (resulting in a stiffer rear and a softer fore section) shifts the deformation wave toward upstream and induces a larger snapping amplitude in the sheet's fore part. Varying ΔEI^* has a remarkable impact on the energy-harvesting performance. Specifically, increasing ΔEI^* shortens the sheet's oscillation period, accelerates the vibration, and consequently enhances kinetic energy harvesting. The potential energy peaks at $\Delta EI^* = 1$, whereas the total energy reaches its maximum value at $\Delta EI^* = 2$. Compared with a configuration in which the fore portion is stiff and the rear portion soft ($\Delta EI^* = -3.9$), the performance is improved in terms of both potential energy and kinetic energy for a configuration with a stiffer rear portion and a softer fore portion ($\Delta EI^* = 3.9$).
3. Increasing the length ratio ΔL^* intensifies the vortex strength, enhances the interaction between sheet and fluid, and consequently effectively increases the potential energy. An optimal precompression length $\Delta L^* = 0.4$ is identified for which both total energy and potential energy are maximized in the current configuration. Notably, the potential energy at $\Delta L^* = 0.4$ is three times higher than that at $\Delta L^* = 0.1$. When $\Delta L^* = 0.5$, the sheet's snap-through motion is totally suppressed. As for the effect of ΔEI^*, when $\Delta L^* < 0.3$, the stiffness pattern of $\Delta EI^* = 2$ increases the total energy, while $\Delta EI^* = -2$ suppresses total energy extraction. However, for $\Delta L^* > 0.3$, both $\Delta EI^* = -2$ and 2 reduce the energy harvesting. The enhancement of potential energy $\overline{E}_p^*$ at $\Delta EI^* = 2$ is effective when $\Delta L^* < 0.2$.

This study has not explicitly investigated the electrical output generated by a snapping sheet, nor has it described the transduction process and the equations pertaining to the electrical circuitry. Rather, the emphasis here has been on the potential and kinetic energies as measures of the harvestable energy. Nevertheless, the study provides valuable insight into the energy harvesting potential of a snapping sheet, taking into account the full fluid–structure interaction. Future work will introduce electrical circuits to evaluate performance in terms of electrical power output.

SUPPLEMENTARY MATERIAL

The supplementary material encompasses instantaneous vorticity contours for the sheet of $\Delta L^* = 0.3$ at $\Delta EI^* = -3.9$, -2, 0, 2, and 3.9.

AUTHOR DECLARATIONS

Conflict of Interest

The authors have no conflicts to disclose.

Author Contributions

Zhaokun Wang: Conceptualization (lead); Data curation (lead); Formal analysis (lead); Investigation (lead); Methodology (lead); Software (lead); Validation (lead); Visualization (lead); Writing – original draft (lead); Writing – review & editing (lead). **Jingyu Cui**: Conceptualization (equal); Data curation (equal); Formal analysis (equal); Investigation (equal); Methodology (equal); Project administration (equal); Validation (equal); Visualization (equal); Writing – review & editing (equal). **Fuwang Zhao**: Conceptualization (equal); Formal analysis (equal); Investigation (lead); Methodology (equal);

Resources (equal); Supervision (lead); Validation (equal); Writing – original draft (equal); Writing – review & editing (lead). **M. N. Mumtaz Qadri**: Conceptualization (equal); Data curation (equal); Investigation (equal); Resources (equal); Software (equal); Supervision (lead); Validation (equal); Writing – original draft (equal); Writing – review & editing (equal). **Yuanye Zhou**: Conceptualization (equal); Formal analysis (equal); Methodology (equal); Project administration (equal); Software (equal); Supervision (lead); Writing – original draft (equal); Writing – review & editing (lead). **Hui Tang**: Conceptualization (equal); Formal analysis (equal); Funding acquisition (equal); Investigation (lead); Methodology (lead); Resources (equal); Software (equal); Validation (equal); Writing – original draft (equal); Writing – review & editing (lead).

DATA AVAILABILITY

The data that support the findings of this study are available from the corresponding author upon reasonable request.

REFERENCES

[1]Y. Zhang, Y. Wang, Y. Xie, G. Sun, and J. Han, "Effects of flexibility on energy extraction performance of an oscillating hydrofoil under a semi-activated mode," Energy **242**, 122940 (2022).

[2]E. Segura, R. Morales, J. Somolinos, and A. López, "Techno-economic challenges of tidal energy conversion systems: Current status and trends," Renewable Sustainable Energy Rev. **77**, 536–550 (2017).

[3]J. Knight, "Breezing into town," Nature **430**, 12–13 (2004).

[4]Y. Cha, H. Kim, and M. Porfiri, "Energy harvesting from underwater base excitation of a piezoelectric composite beam," Smart Mater. Struct. **22**, 115026 (2013).

[5]M. Nachtane, M. Tarfaoui, I. Goda, and M. Rouway, "A review on the technologies, design considerations and numerical models of tidal current turbines," Renewable Energy **157**, 1274–1288 (2020).

[6]F. Zhao, M. N. Mumtaz Qadri, Z. Wang, and H. Tang, "Flow-energy harvesting using a fully passive flapping foil: A guideline on design and operation," Int. J. Mech. Sci. **197**, 106323 (2021).

[7]H.-X. Zou *et al.*, "A self-regulation strategy for triboelectric nanogenerator and self-powered wind-speed sensor," Nano Energy **95**, 106990 (2022).

[8]J. Bae *et al.*, "Flutter-driven triboelectrification for harvesting wind energy," Nat. Commun. **5**, 4929 (2014).

[9]P. Bearman, "Circular cylinder wakes and vortex-induced vibrations," J. Fluids Struct. **27**, 648–658 (2011).

[10]R. Badhurshah, R. Bhardwaj, and A. Bhattacharya, "Energy extraction via Vortex-Induced Vibrations: The effect of spring bistability," J. Fluids Struct. **114**, 103708 (2022).

[11]J. Kim, H. Kim, and D. Kim, "Snap-through oscillations of tandem elastic sheets in uniform flow," J. Fluids Struct. **103**, 103283 (2021).

[12]F. Zhao *et al.*, "Interaction of two fully passive flapping foils arranged in tandem and its influence on flow energy harvesting," Energy **268**, 126714 (2023).

[13]F. Zhao *et al.*, "Effects of wake interaction on energy extraction performance of tandem semi-active flapping foils," Phys. Fluids **35**, 087112 (2023).

[14]M. M. Bernitsas, K. Raghavan, Y. Ben-Simon, and E. Garcia, "VIVACE (vortex induced vibration aquatic clean energy): A new concept in generation of clean and renewable energy from fluid flow," J. Offshore Mech. Arct. Eng. **130**, 041101 (2008).

[15]M. M. Bernitsas, *Springer Handbook of Ocean Engineering* (Springer, 2016), pp. 1163–1244.

[16]B. H. Huynh, T. Tjahjowidodo, Z.-W. Zhong, Y. Wang, and N. Srikanth, "Design and experiment of controlled bistable vortex induced vibration energy harvesting systems operating in chaotic regions," Mech. Syst. Signal Process. **98**, 1097–1115 (2018).

[17]Y. Lv, L. Sun, M. M. Bernitsas, and H. Sun, "A comprehensive review of nonlinear oscillators in hydrokinetic energy harnessing using flow-induced vibrations," Renewable Sustainable Energy Rev. **150**, 111388 (2021).

[18]L. Duarte, N. Dellinger, G. Dellinger, A. Ghenaim, and A. Terfous, "Experimental investigation of the dynamic behaviour of a fully passive flapping foil hydrokinetic turbine," J. Fluids Struct. **88**, 1–12 (2019).

[19]J. Wang, L. Geng, L. Ding, H. Zhu, and D. Yurchenko, "The state-of-the-art review on energy harvesting from flow-induced vibrations," Appl. Energy **267**, 114902 (2020).

[20]A. K. Soti, J. Zhao, M. C. Thompson, J. Sheridan, and R. Bhardwaj, "Damping effects on vortex-induced vibration of a circular cylinder and implications for power extraction," J. Fluids Struct. **81**, 289–308 (2018).

[21]F. Zhao, Z. Wang, H. Bai, and H. Tang, "Energy harvesting based on flow-induced vibration of a wavy cylinder coupled with tuned mass damper," Energy **282**, 128584 (2023).

[22]F. Zhao *et al.*, "Effects of superhydrophobicity on VIV control of a circular cylinder," Appl. Phys. Lett. **123**, 101603 (2023).

[23]A. Mackowski and C. Williamson, "An experimental investigation of vortex-induced vibration with nonlinear restoring forces," Phys. Fluids **25**, 087101 (2013).

[24]E. Wang *et al.*, "The effect of cubic stiffness nonlinearity on the vortex-induced vibration of a circular cylinder at low Reynolds numbers," Ocean Eng. **173**, 12–27 (2019).

[25]B. H. Huynh, T. Tjahjowidodo, Z. Zhong, Y. Wang, and N. Srikanth, in *2015 IEEE International Conference on Advanced Intelligent Mechatronics (AIM)* (IEEE, 2015), pp. 91–96.

[26]H. Sun, C. Ma, and M. M. Bernitsas, "Hydrokinetic power conversion using Flow Induced Vibrations with cubic restoring force," Energy **153**, 490–508 (2018).

[27]R. Ramlan, M. J. Brennan, B. R. Mace, and I. Kovacic, "Potential benefits of a non-linear stiffness in an energy harvesting device," Nonlinear Dyn. **59**, 545–558 (2010).

[28]L.-Q. Chen and K. Li, "Equilibriums and their stabilities of the snap-through mechanism," Arch. Appl. Mech. **86**, 403–410 (2016).

[29]R. Badhurshah, R. Bhardwaj, and A. Bhattacharya, "Lock-in regimes for vortex-induced vibrations of a cylinder attached to a bistable spring," J. Fluids Struct. **91**, 102697 (2019).

[30]R. Badhurshah, R. Bhardwaj, and A. Bhattacharya, "Numerical simulation of Vortex-Induced Vibration with bistable springs: Consistency with the Equilibrium Constraint," J. Fluids Struct. **103**, 103280 (2021).

[31]R. L. Harne and K. Wang, "A review of the recent research on vibration energy harvesting via bistable systems," Smart Mater. Struct. **22**, 023001 (2013).

[32]L. Zhang, A. Abdelkefi, H. Dai, R. Naseer, and L. Wang, "Design and experimental analysis of broadband energy harvesting from vortex-induced vibrations," J. Sound Vib. **408**, 210–219 (2017).

[33]Z. Zhou, W. Qin, P. Zhu, and S. Shang, "Scavenging wind energy by a Y-shaped bi-stable energy harvester with curved wings," Energy **153**, 400–412 (2018).

[34]B. Huynh and T. Tjahjowidodo, "Experimental chaotic quantification in bistable vortex induced vibration systems," Mech. Syst. Signal Process. **85**, 1005–1019 (2017).

[35]J. Casals-Terre, A. Fargas-Marques, and A. M. Shkel, "Snap-action bistable micromechanisms actuated by nonlinear resonance," J. Microelectromech. Syst. **17**, 1082–1093 (2008).

[36]M. Gomez, D. E. Moulton, and D. Vella, "Passive control of viscous flow via elastic snap-through," Phys. Rev. Lett. **119**, 144502 (2017).

[37]H. Kim, Q. Zhou, D. Kim, and I.-K. Oh, "Flow-induced snap-through triboelectric nanogenerator," Nano Energy **68**, 104379 (2020).

[38]D. N. Betts, H. A. Kim, C. R. Bowen, and D. Inman, "Optimal configurations of bistable piezo-composites for energy harvesting," Appl. Phys. Lett. **100**, 114104 (2012).

[39]Z. Wang *et al.*, "Towards energy harvesting through flow-induced snap-through oscillations," Int. J. Mech. Sci. **254**, 108428 (2023).

[40]Z. Wang, F. Zhao, B. Xu, L. Zeng, and H. Tang, "Effect of boundary conditions on energy harvesting of a flow-induced snapping sheet at low Reynolds number," Phys. Fluids **35**, 127103 (2023).
[41]L. Long, Z. Wang, and K. Chen, "Analysis of the hollow structure with functionally gradient materials of moso bamboo," J. Wood Sci. **61**, 569–577 (2015).
[42]D. Floryan and C. W. Rowley, "Distributed flexibility in inertial swimmers," J. Fluid Mech. **888**, A24 (2020).
[43]W. Wang, H. Huang, and X.-Y. Lu, "Optimal chordwise stiffness distribution for self-propelled heaving flexible plates," Phys. Fluids **32**, 111905 (2020).
[44]W. Wang, H. Huang, and X.-Y. Lu, "Interplay of chordwise stiffness and shape on performance of self-propelled flexible flapping plate," Phys. Fluids **33**, 091904 (2021).
[45]B. S. Connell and D. K. Yue, "Flapping dynamics of a flag in a uniform stream," J. Fluid Mech. **581**, 33–67 (2007).
[46]R.-N. Hua, L. Zhu, and X.-Y. Lu, "Locomotion of a flapping flexible plate," Phys. Fluids **25**, 121901 (2013).
[47]C. Wang and H. Tang, "Influence of complex driving motion on propulsion performance of a heaving flexible foil," Bioinspiration Biomimetics **14**, 016011 (2018).
[48]C. Wang and H. Tang, "On the aeroelastic energy transfer from a Lamb dipole to a flexible cantilever," J. Fluids Struct. **86**, 170–184 (2019).
[49]S. K. Kang, *Immersed Boundary Methods in the Lattice Boltzmann Equation for Flow Simulation* (Texas A&M University, 2010).
[50]J. Cui, Z. Wang, Y. Liu, Y. Jin, and Z. Zhu, "Three-dimensional simulation of lateral migration of fiber in a laminar channel flow," Int. J. Mech. Sci. **236**, 107766 (2022).
[51]Z. Guo, C. Zheng, and B. Shi, "Discrete lattice effects on the forcing term in the lattice Boltzmann method," Phys. Rev. E **65**, 046308 (2002).
[52]P. Lallemand and L.-S. Luo, "Theory of the lattice Boltzmann method: Dispersion, dissipation, isotropy, Galilean invariance, and stability," Phys. Rev. E **61**, 6546 (2000).
[53]L.-S. Luo, W. Liao, X. Chen, Y. Peng, and W. Zhang, "Numerics of the lattice Boltzmann method: Effects of collision models on the lattice Boltzmann simulations," Phys. Rev. E **83**, 056710 (2011).
[54]J. F. Doyle, *Nonlinear Analysis of Thin-Walled Structures: Statics, Dynamics, and Stability* (Springer Science & Business Media, 2013).
[55]M. Schulz and F. C. Filippou, "Non-linear spatial Timoshenko beam element with curvature interpolation," Int. J. Numer. Methods Eng. **50**, 761–785 (2001).
[56]R. M. De Souza, *Force-Based Finite Element for Large Displacement Inelastic Analysis of Frames* (University of California, Berkeley, 2000).
[57]M. A. Crisfield, "A consistent co-rotational formulation for non-linear, three-dimensional, beam-elements," Comput. Methods Appl. Mech. Eng. **81**, 131–150 (1990).
[58]Z. Wang *et al.*, "Fluid-structure interaction in phaco-emulsification based cataract surgery," Int. J. Mech. Sci. **267**, 109022 (2024).
[59]Z. Wang *et al.*, "Simulation of fluid–structure interaction during the phaco-emulsification stage of cataract surgery," Int. J. Mech. Sci. **214**, 106931 (2022).
[60]C. S. Peskin, "The immersed boundary method," Acta Numer. **11**, 479–517 (2002).
[61]S. P. Timoshenko and J. M. Gere, *Theory of Elastic Stability* (Courier Corporation, 2009).
[62]H. Kim, M. Lahooti, J. Kim, and D. Kim, "Flow-induced periodic snap-through dynamics," J. Fluid Mech. **913**, A52 (2021).
[63]I. Lee and H. Choi, "A discrete-forcing immersed boundary method for the fluid–structure interaction of an elastic slender body," J. Comput. Phys. **280**, 529–546 (2015).